Mesoscopic superconducting memory based on bistable magnetic textures

Fermin, R.; Scheinowitz, N.M.A.; Aarts, J.; Lahabi, K.

Mesoscopic superconducting memory based on bistable magnetic textures

R. Fermin [1], N. M. A. Scheinowitz [1], J. Aarts [1], and K. Lahabi [1,2,*]

[1] *Huygens-Kamerlingh Onnes Laboratory, Leiden University, P.O. Box 9504, 2300 RA Leiden, The Netherlands*

[2] *Department of Quantum Nanoscience, Kavli Institute of Nanoscience, Delft University of Technology, 2628 CJ Delft, The Netherlands*

(Received 28 January 2022; accepted 8 July 2022; published 19 August 2022)

With the ever-increasing energy need to process big data, the realization of low-power computing technologies, such as superconducting logic and memories, has become a pressing issue. Developing fast and nonvolatile superconducting memory elements, however, remains a challenge. Superconductor-ferromagnet hybrid devices offer a promising solution, as they combine ultrafast manipulation of spins with dissipationless readout. Here, we present a type of nonvolatile Josephson junction memory that utilizes the bistable magnetic texture of a single mesoscopic ferromagnet. We use micromagnetic simulations to design an ellipse-shaped planar junction structured from a Co/Nb bilayer. The ellipse can be prepared as uniformly magnetized or as a pair of vortices at zero applied field. The two states yield considerably different critical currents, enabling reliable electrical readout of the element. We describe the mechanism that controls the critical current by applying numerical calculations to quantify the local stray field from the ferromagnet, which shifts the superconducting interference pattern. Our approach presents a route towards realizing superconducting memory applications by combining micromagnetic modeling with bistable spin-textured junctions.

DOI: 10.1103/PhysRevResearch.4.033136

I. INTRODUCTION

In recent years, energy-hungry data centers have accounted for more than 1% of the global electricity consumption; this number is projected to increase to 3–13% by 2030 [1]. As data centers are already responsible for 0.3% of the overall carbon emissions, the development of low-power supercomputers has become an immediate global concern [2]. Due to their nondissipative nature, superconducting logic and memory devices present a tantalizing route to address this issue, promising enormous savings, even accounting for cryogenic cooling [3–7]. While several classes of high-performance superconducting processors already exist, cryogenic memories remain relatively underdeveloped and far from meeting their applications. Nonvolatility and scalability, in particular, have been the major obstacles in the industrial realization of superconducting memories.

The combination of superconducting (S) and ferromagnetic (F) elements can tackle the nonvolatility issue through S/F/S devices, in which different (stable) magnetic configurations yield different critical supercurrents. Much work has been done on stacked magnetic Josephson junctions with a weak ferromagnetic barrier, where small magnetic field pulses could switch the critical current [8–11]. However, the weak ferromagnet used in such systems has a typically low Curie temperature (around 10 K), limiting their non-volatility. Josephson memories have also been extensively studied in so-called pseudo-spin-valve (S/F/N/F′/S) devices, where the magnetization of two ferromagnetic layers, separated by a normal metal (N), could be set parallel or antiparallel to yield a change in critical current [12–18]. The work on pseudo spin valves has also been extended to multilayer Josephson devices featuring triplet supercurrents, which not only carry charge but also carry spin [19,20]. Finally, all-oxide devices, which can operate at high temperatures, were recently examined [21]. In general, the existing nonvolatile Josephson memories utilize an intricate layer set and face a number of obstacles, such as interlayer coupling between magnetic layers and stochastic distribution of magnetic flux in the junction. Other problems include insufficient contrast between states for electrical readout and the requirement for applying a large writing field.

To address these challenges, we present an alternative route for developing nonvolatile Josephson memory elements, where information is stored by the spin texture of a single mesoscopic ferromagnet. Magnetic textures, in general, and specifically ferromagnetic vortices, can be manipulated by applying pulsed microwave radiation, leading to the realization of ultrafast electronics [22–24]. Combining information inscription in spin textures with the nondissipative nature of supercurrents can thus lead to the realization of high-speed, low-power, and nonvolatile memory elements. The synergy between superconductivity and magnetic textures is amplified further by allowing for triplet supercurrents, paving the road for superconducting spintronics [25–27]. Textured superconductor-ferromagnet hybrid devices therefore open an alternative paradigm in superconducting memory applications.

Here, we show the realization of a micrometer-sized superconducting memory element based on bistable spin textures in the F layer of an elliptical planar S/F/S Josephson junction. By combining micromagnetic simulations with

*lahabi@physics.leidenuniv.nl

nanostructured hybrid devices, we are able to control the transport behavior of our devices with their magnetic texture. By applying a magnetic field of 40 mT for the writing operation, we can reliably switch between two stable spin textures: One is uniformly magnetized, and the other hosts a pair of ferromagnetic vortices. These correspond to a minimum and a maximum critical supercurrent of the junction, respectively. We obtain a factor-of-5 difference in the critical current between the two states, which allows for a facile and reliable electrical readout of the element. By quantifying the local stray field from the ferromagnet, we show that the difference in critical current is caused by a shift in the superconducting interference pattern. Moreover, the magnetic bistability enables us to use writing fields that are considerably smaller than the local stray field from the ferromagnet. We confirm that the memory is stable, nonvolatile, and nondestructive upon readout.

II. RESULTS AND DISCUSSION

A. Ellipse-shaped S/F/S junctions

A bilayer of cobalt (65 nm) and niobium (50 nm) is deposited in an ultrahigh vacuum by Ar sputtering on a four-probe geometry lift-off pattern. Elliptic S/F/S devices are structured from the Co/Nb bilayer using focused ion beam milling. Figure 1 shows a false-color scanning electron micrograph of such an ellipse-shaped device, having dimensions of 1500 × 750 nm (long and short axes, respectively). Micromagnetic simulations show that the zero-field spin texture of such devices is expected to be bistable: Either the cobalt layer is magnetized along the long axis of the ellipse (we call this the M state) or two ferromagnetic vortices are stable near each focal point of the ellipse (V state). We depict simulation results from these states in Fig. 1(b). The full technical details of the simulations are presented in the Appendix. Essentially, this allows for writing a bit with the value "0" (M state) or "1" (V state) into the spin texture of the device. We prepare the states by first applying a 40 mT in-plane field either parallel to the long axis or parallel to the short axis of the devices. Next, after removing the field along the short (long) axis, the V state (M state) is stable in the device.

Using ultralow ion beam currents, We fabricate a planar Josephson junction in the ellipse by locally removing the Nb top layer. This creates an approximately 20-nm-wide trench, separating the Nb contacts and forcing the supercurrent through the ferromagnet. Planar S/F/S junctions fabricated in this manner were used to study triplet supercurrents in previous works [28,29]. The trench is positioned near the focal point of the ellipse, which corresponds to the approximate location of one of the vortex cores in the V state. As discussed later, this particular location is designed to optimize the stray-field-driven mechanism that assigns different critical currents to the M and V states. In this paper, we describe two of these elliptical devices (devices A and B), although all observations are repeated for a large number of samples. For additional data, the reader is referred to Sec. S1 of the Supplemental Material [30]. The sample resistance is measured using a dc source (Keithley 6221) and a voltmeter (Keithley 2182A) in a four-probe fashion, where the voltage

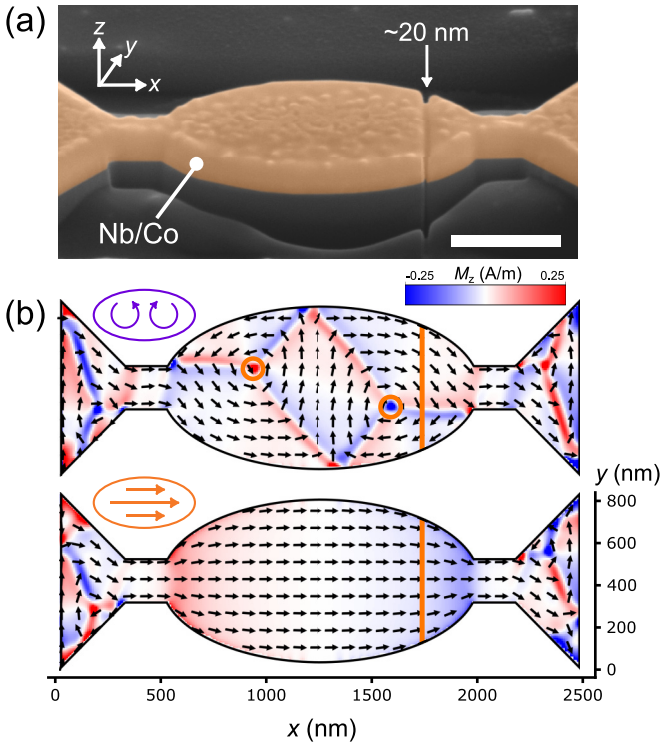

FIG. 1. (a) False-color scanning electron micrograph of the ellipse-shaped S/F/S junction device A. The Co weak link is formed by the indicated trench (∼20 nm in size) that separates the two Nb electrodes. The scale bar corresponds to 500 nm. (b) The simulated bistable spin textures at zero field. The cobalt either is magnetized along the long axis of the device (M state) or hosts two stable vortices (V state). Orange circles highlight the vortex cores, and the orange line indicates the trench location. The color scale indicates the out-of-plane magnetization of the top of the cobalt layer.

drop over the bar-shaped contacts as well as the ellipse is measured. Figure 2 shows the resistance R versus temperature T of device A, measured with a current of 20 μA. If the sample is prepared in the V state, we find two transitions. The first corresponds to the bulk superconducting transition temperature T_c of the Nb layer, and the second is due to the superconducting proximity effect in the S/F/S junction formed by the trench. In contrast, the M state does not show a second transition, indicating that the critical current I_c of the junction in this state is suppressed to below the measurement current. This difference in I_c between the two states allows us to electrically read out the magnetic state of the memory element. To unambiguously demonstrate the superconducting proximity effect in our devices, we show the appearance of Shapiro steps in the current-voltage (IV) characteristic of device A under the application of radio frequency (rf) radiation, which is supplied by a nearby antenna. We carry out these measurements at 1.6 K in the V state. The step height in the IV characteristic shown in Fig. 2(b) is in units of $hf/2e$ (where h is the Planck constant, f is the frequency of the rf radiation, and e is the electron charge), confirming the Shapiro response.

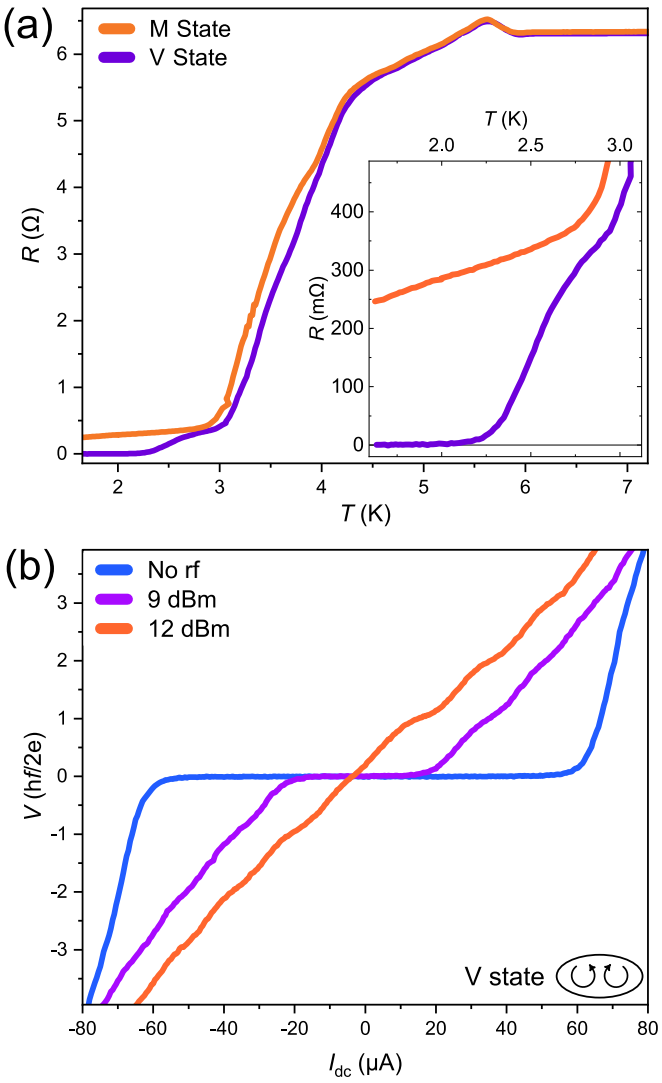

FIG. 2. Basic transport characteristics of device A. In (a) we show the resistance-vs-temperature curves for both the M state and the V state, measured using 20 μA current bias. The critical current is suppressed below 20 μA in the M state. The inset shows the low-temperature behavior. (b) depicts three IV characteristics of the sample in the V state, acquired under different rf radiation powers. The frequency is 1.6 GHz, and the temperature is 1.6 K. The measured voltage is normalized to $hf/2e$ and shows a clear Shapiro response.

B. Controllable switching

To show the bistability of the spin textures, we examine the dependence of I_c on the in-plane "writing" fields H_x and H_y along the long and the short axis of the ellipse, respectively. The results are shown in Figs. 3(a) and 3(b), accompanied by the simulated spin textures. If the sample is in the M state ("0"), I_c is 5 μA. The datum "1" can be written by increasing the field along the short axis of the ellipse. At a field of 40 mT, I_c grows to above 20 μA, which is accompanied by a buckling of the simulated spin texture. Upon decreasing the field to zero, the high-I_c state is retained, and the buckled spin texture evolves into two vortices. Therefore the device is converted into the V state ("1"). Conversely, the M state can be written in the device by applying a field parallel to the long axis of the ellipse. The field effectively displaces the vortices towards the edges of the sample. At a field of 15 mT, they are fully pushed out from the ellipse, and the spins align in the M state. This is accompanied by a drop in I_c back to 5 μA. The low I_c is stable upon decreasing the field back to zero in the M state.

Figures 3(c) and 3(d) show the total energy associated with the simulated spin texture as a function of the externally applied field (i.e., the sum of the exchange, demagnetization, and Zeeman energies). Two branches can be discerned corresponding to the two states, both stable at zero field. In the simulations, the buckled state, which is required to stabilize of the V state, appears above 45 mT. During the converse switching operation, a field of 25 mT is required to magnetize the ellipse. Remarkably, we find that both switching fields closely follow the experimental values with only a small offset, which can be attributed to the reduced geometry of the contacts and the finite field steps used in the simulations.

We examine the performance of our devices by repeatably switching them between the two states while studying the transport behavior. Figure 4(a) shows the zero-field IV characteristic of the two states. Based on the difference in I_c, we can define a readout current corresponding to a finite voltage in the M state, but a zero voltage in the V state. We cycle the device between the two states (using a 40 mT field) and acquire the voltage at the readout current in each state. In Fig. 4(b), we show a histogram of the measured voltage at a readout current of 30 μA, totaling 78 subsequent writing cycles. There is no overlap in the histogram, making the states highly distinguishable. As the readout current density is far too low to alter the spin texture, the readout operation is fully nondestructive. Furthermore, by heating the ellipse to above the T_c of the superconducting layer between subsequent write and read operations, we confirm the nonvolatility of its memory. This was found to hold, even when the sample is warmed to room temperature and stored for days. Additionally, to test the resilience to perturbations of the spin texture, we try to cycle between the states using a field of 10 mT. We find these fields to be insufficient to alter I_c, demonstrating the stability of our devices.

C. Stray-field-driven mechanism

We now discuss the mechanism used for suppressing the I_c in the M state, based on the local stray field emerging from the ferromagnet. To illustrate this, we perform superconducting quantum interference (SQI) measurements, where we sweep the out-of-plane field and acquire an IV characteristic at each field. During the SQI measurements, we obtain a direct measure of dV/dI, by obtaining an ac voltage using a Synk-Tek MCL1-540 multichannel lock-in. For a regular junction, the interference pattern $I_c(B)$ corresponds to the well-known Fraunhofer pattern. Note that the magnitude of the out-of-plane fields is insufficient to alter the global spin texture of the device (i.e., the out-of-plane fields cannot transform the M state into the V state or vice versa). We present such SQI measurements, obtained on device B, for the V state and the left- and right-magnetized M state in the color maps of Figs. 5(a)–5(c). For this sample, we observe a pattern with a single middle lobe and heavily suppressed side lobes [31].

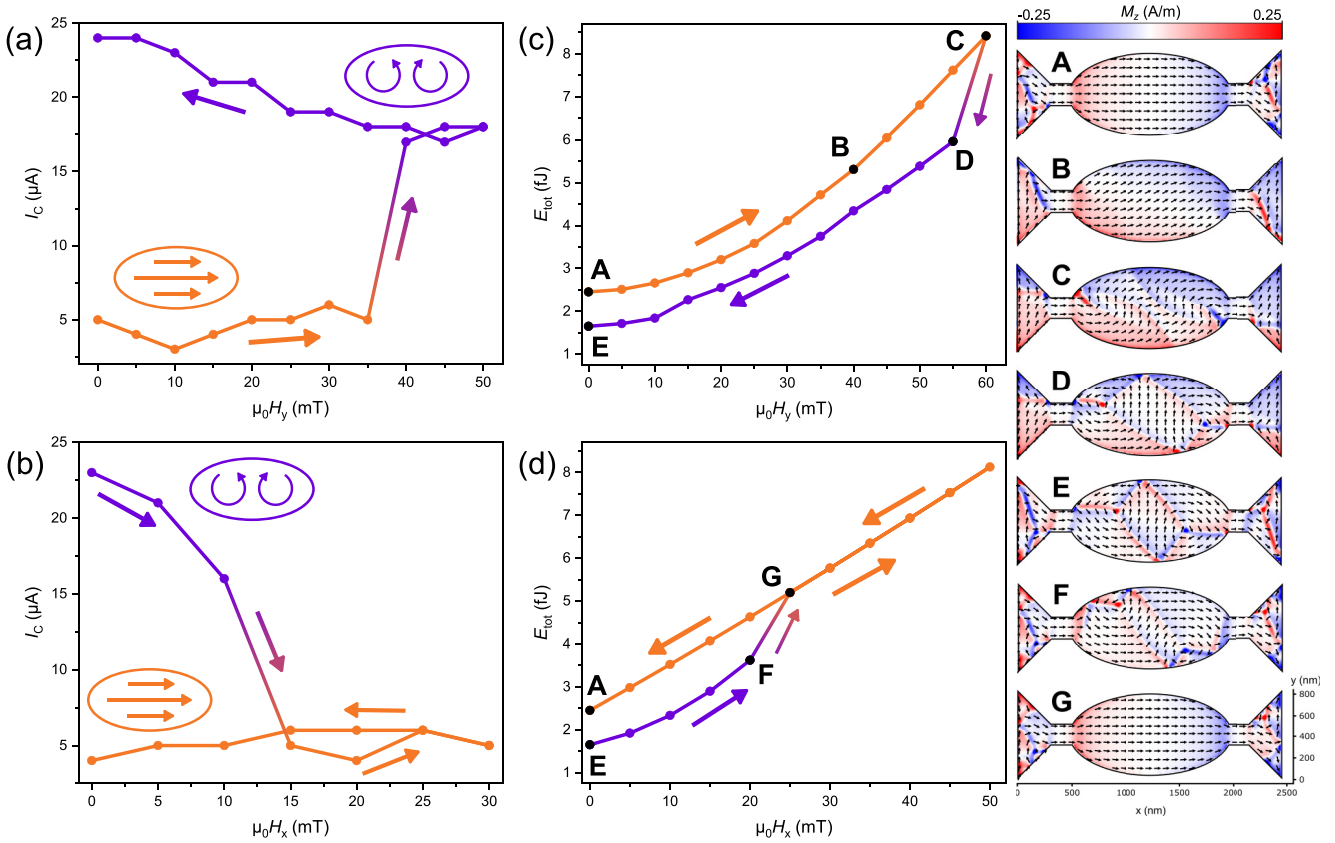

FIG. 3. The critical current I_c, the total simulated energy E_{tot}, and the spin texture of the device as a function of H_x (field along the long axis) and H_y (along the short axis). Results were obtained on device B at 1.7 K. (a) and (b) depict $I_c(H_y)$ and $I_c(H_x)$. In (a) the field is increased along the short axis of the ellipse. At 40 mT, I_c increases sharply, effectively transforming the M state into the V state. The reverse operation is shown in (b): By increasing the field—parallel to the long axis of the ellipse—to 15 mT, the critical current drops to 5 μA, bringing the device back to the M state. (c) and (d) show E_{tot} corresponding to the in-plane field sweeps. Two branches can be seen in both panels, corresponding to the V and M states. A change in magnetic state coincides with a jump from one branch to the other. We are able to predict the switching fields within a small error correctly. The panel to the right of (c) and (d) contains snapshots of the spin texture during the simulated field sweeps. Here, the color scale indicates the magnetization of the top of the Co layer.

For the V state [Fig. 5(c)], the pattern is centered at zero field. By switching to either of the M states [Figs. 5(a) and 5(b)], the shape of the SQI pattern is not altered; yet it is clearly shifted by around 60 mT from zero applied field. Moreover, the magnetization direction in the M state determines the sign of this shift. Therefore it is evident that the suppressed I_c of the M state is a result of the local stray fields from the Co layer, introducing a shift in the $I_c(B)$ pattern. However, what makes our spin-textured devices truly stand out from previous Josephson memory elements is that we use a writing field (40 mT) that is noticeably smaller than the resulting shift (60 mT).

In the following, we describe how the pattern shift can be quantified by simulating the stray flux entering the junction. We sum the z component of the flux—evaluated in a thin sheet above the cobalt layer—over an integration window to obtain the local stray fields threading the area of the window. The size of this window is chosen to reflect the trench area, yielding an estimate of the stray fields penetrating the junction. A more extensive discussion of obtaining the stray fields is presented in Sec. S2 of the Supplemental Material [30]. Figure 5(d) displays the simulated (stray-field-induced) pattern shift as a function of the window location; the vertical line indicates the location of the trench in the actual sample. This shows that the V state corresponds to negligible stray fields at the junction, accounting for the centered pattern in Fig. 5(c) with no offset. The M state corresponds to an 80-mT shift, which closely follows the 60-mT offset in the SQI patterns. Note that the simulated stray field is symmetric with respect to the center of the sample. This reflects the sign change that occurs when the magnetization direction is reversed.

Note that the spin texture snapshots of Fig. 3 show the source of the stray fields. In the M state, the ellipse features a dipolelike field along its long axis, which is absent in the V state. We do observe some stray fields in the V state; however, these average out over the junction area. Therefore the total shift in the SQI pattern remains zero. During the field sweep along the short axis of the ellipse (i.e., the switch from M state to V state), the spin texture buckles before two vortices stabilize, as can be seen in snapshots B and C in Fig. 3. When this buckling occurs, the dipolelike field no longer points along the long axis of the ellipse, and consequently, the stray

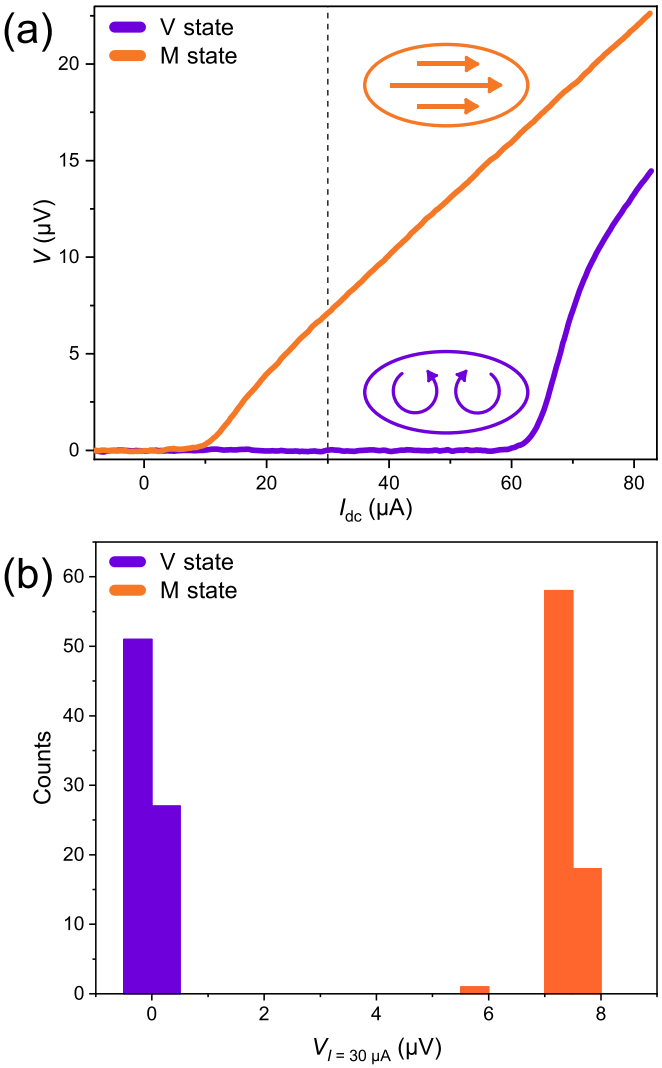

FIG. 4. Fidelity of the writing cycles of device A. The *IV* characteristics of the two states, measured at 1.6 K, are shown in (a). Based on these curves, we define a readout current corresponding to a finite voltage in the M state and zero voltage in the V state. We cycle the device between the two states 78 times and measure the voltage before each subsequent switch. (b) shows a histogram of the readout voltages, measured using a 30 μA current [the dashed line in (a)].

fields average out over the junction area. This explains why the high-I_c state occurs before two vortices enter the ellipse.

D. Pairing symmetry of the supercurrents

In previous work on similar S/F/S junctions with a circular geometry—containing a single ferromagnetic vortex—we found spin texture to be a prerequisite for the superconducting proximity effect, which led to the conclusion that the transport in these disk-shaped S/F/S junctions is dominated by long-range triplet (LRT) Cooper pairs [28,29]. Contrary to conventional Cooper pairs, these LRT pairs consist of spin-polarized electrons that can penetrate a ferromagnet over far longer length scales (up to hundreds of nanometers in a half metal) [26,32–34].

In this case, however, we cannot be certain about the LRT scenario. Due to the similarity to the circular devices, LRT correlations can be expected in the V state of the ellipse-shaped devices described here. However, there are a number of inconsistencies; the most notable ones are discussed here. Firstly, unlike with the disk-shaped devices, removing the spin texture from our junctions does not suppress the proximity effect, i.e., the maximum of $I_c(B)$ values for both the M state and the V state are quite similar. Secondly, while the SQI patterns of the disk-shaped devices are highly sensitive to the subtle changes in the spin texture, the elliptic junctions show the same type of pattern for widely different magnetic states. Both of these observations seem to counter the notion of the LRT correlations and indicate that transport in the elliptic junctions is carried by the short-range triplet correlations instead (i.e., Cooper pairs with no spin projection). However, one could argue that even the M state still features some spin texture near the edges of the sample [due to the tapered shape of the ellipse; see Fig. 1(b)], which possibly allows for the generation of LRT correlations. Finally, the similar SQI patterns between the magnetic states can possibly be caused by the relatively short junction width [35]. At this stage, no conclusions can be drawn on the triplet or singlet nature of the supercurrents in our devices, and further experiments are necessary. We emphasize, however, that the mechanism for the shift in the SQI patterns (i.e., the stray fields) holds for both singlet and triplet pairing symmetries.

III. CONCLUSION AND OUTLOOK

We demonstrate the realization of a nonvolatile superconducting memory element based on magnetic textures in an S/F/S Josephson junction. The ellipsoidal shape of the device leads to two stable magnetic states at zero applied magnetic field: a fully magnetized state and a state containing ferromagnetic vortices. These can be associated with the data "0" and "1," respectively. By applying and removing an externally applied in-plane field, we can reliably switch between these states, performing a write operation. We find a strong suppression of the critical current in the magnetized state, which allows for a nondestructive determination of the spin state and therefore electrical readout of the bit. By combining transport experiments and micromagnetic simulations, we show that the difference in critical current between the two states results from internal stray fields originating from the ferromagnetic layer of the device, which creates a local offset field in the junction. Since the ferromagnetic textures can be controllably manipulated with rf radiation, storing information in mesoscopic superconductor-ferromagnet devices can provide an exciting avenue for realizing ultrafast electronics. Besides, strain-mediated switching of similar elliptical devices has been recently theoretically studied and shown to be a good alternative to switching using externally applied fields [36]. Combined with the possibility of long-range triplet supercurrents in hybrid devices, the memory devices presented here can form an essential building block for superconducting spintronics.

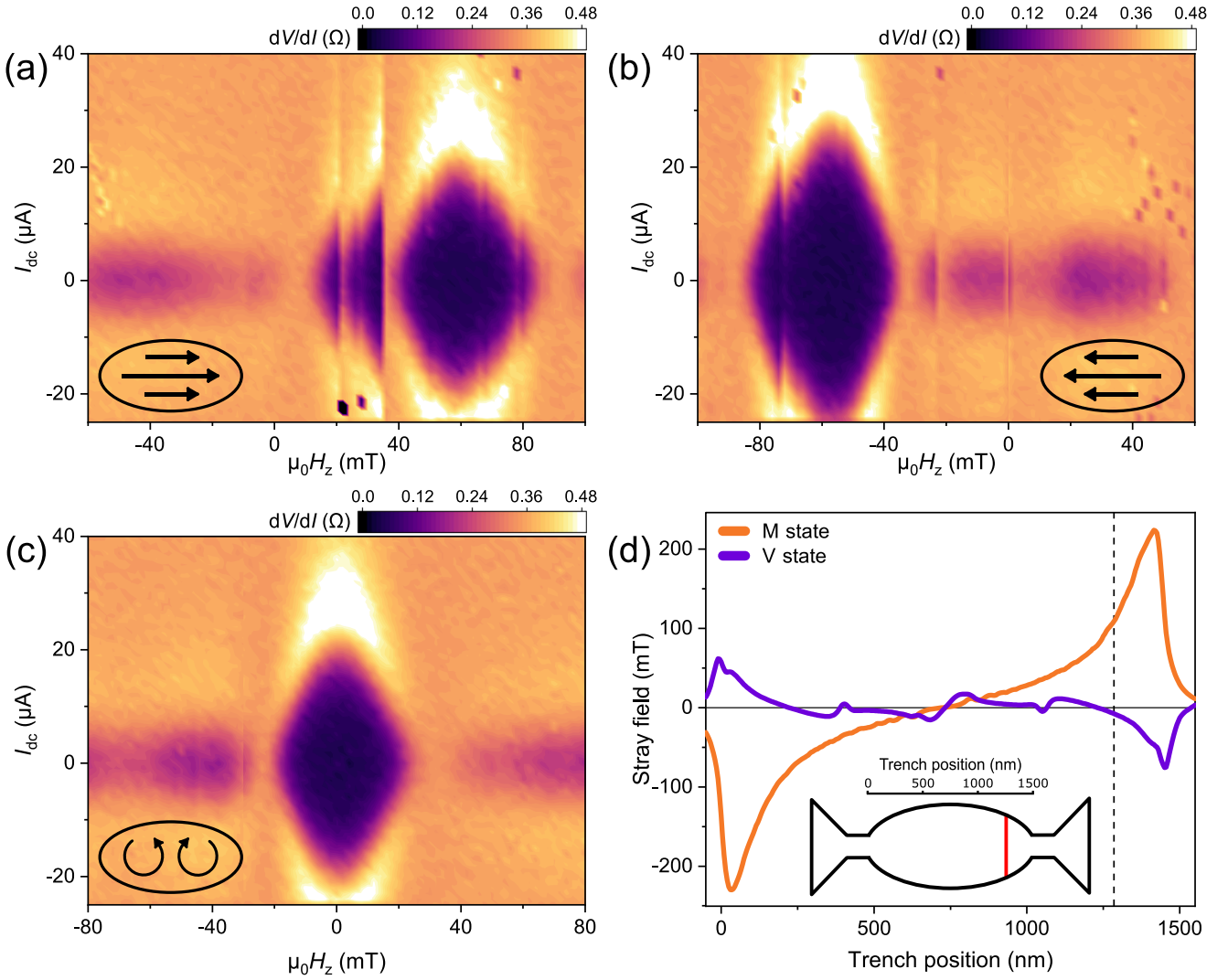

FIG. 5. Stray fields cause a shift in I_c. (a), (b), and (c) show the superconducting interference (SQI) patterns in the right-magnetized M state, the left-magnetized M state, and the V state obtained on device B, respectively. Although the shape of the SQI pattern does not change, the center lobe of the pattern is shifted in the V state with respect to the pattern in the M state (for both magnetizations). Some measurement glitches are visible in (a) and (b). These result from sudden small magnetic configurations in the sample. Stray fields from the ferromagnetic layer cause the shift, as is demonstrated in (d), which shows the simulated field shift for different trench locations. The vertical dashed line in (d) corresponds to the actual location of the trench (see Fig. 1). The inset shows the geometry of the sample with the corresponding scale distribution. The red line indicates the actual location of the trench.

ACKNOWLEDGMENTS

This work was supported by the Dutch Research Council (NWO) as part of the Frontiers of Nanoscience (NanoFront) program and through NWO Projectruimte Grant No. 680.91.128. The work was also supported by EU Cost Action CA16218 (NANOCOHYBRI) and benefited from access to the Netherlands Centre for Electron Nanoscopy (NeCEN) at Leiden University.

APPENDIX: MICROMAGNETIC MODELING

Micromagnetic simulations are performed using the MUMAX3 program [37], which is graphics processing unit (GPU) based. The cobalt layer is divided into a mesh of 5-nm cubic cells. The exchange coefficient is set to 3×10^{-11} J/m, and the saturation magnetization is 1.4×10^{-6} A/m. We choose the Gilbert damping constant to be 0.5, to allow for faster convergence and therefore increased computation speed. As the cobalt film is polycrystalline due to the Ar-sputtering method, we use a zero anisotropy constant. We simulate vacuum cells above the cobalt layer to evaluate the local stray fields emerging from the ferromagnet. These cells feature zero spin; however, they are threaded by a magnetic field flux. Summing the z component of the flux in the vacuum layer over an integration window leads to an expression of the local stray field. The area of the integration window is determined by the local width of the ellipse and a fixed length of 20 nm. This reflects the size of the trench.

[1] A. Andrae and T. Edler, On global electricity usage of communication technology: Trends to 2030, Challenges **6**, 117 (2015).

[2] N. Jones, How to stop data centres from gobbling up the world's electricity, Nature (London) **561**, 163 (2018).

[3] D. S. Holmes, A. L. Ripple, and M. A. Manheimer, Energy-efficient superconducting computing: Power budgets and requirements, IEEE Trans. Appl. Supercond. **23**, 1701610 (2013).

[4] I. I. Soloviev, N. V. Klenov, S. V. Bakurskiy, M. Y. Kupriyanov, A. L. Gudkov, and A. S. Sidorenko, Beyond Moore's technologies: Operation principles of a superconductor alternative, Beilstein J. Nanotechnol. **8**, 2689 (2017).

[5] L. Chen, L. Wu, Y. Wang, Y. Pan, D. Zhang, J. Zeng, X. Liu, L. Ma, W. Peng, Y. Wang, J. Ren, and Z. Wang, Miniaturization of the superconducting memory cell via a three-dimensional Nb nano-superconducting quantum interference device, ACS Nano **14**, 11002 (2020).

[6] B. A. Butters, R. Baghdadi, M. Onen, E. A. Toomey, O. Medeiros, and K. K. Berggren, A scalable superconducting nanowire memory cell and preliminary array test, Supercond. Sci. Technol. **34**, 035003 (2021).

[7] H. Hilgenkamp, Josephson memories, J. Supercond. Novel Magn. **34**, 1621 (2021).

[8] T. I. Larkin, V. V. Bol'ginov, V. S. Stolyarov, V. V. Ryazanov, I. V. Vernik, S. K. Tolpygo, and O. A. Mukhanov, Ferromagnetic Josephson switching device with high characteristic voltage, Appl. Phys. Lett. **100**, 222601 (2012).

[9] I. V. Vernik, V. V. Bol'Ginov, S. V. Bakurskiy, A. A. Golubov, M. Y. Kupriyanov, V. V. Ryazanov, and O. A. Mukhanov, Magnetic Josephson junctions with superconducting interlayer for cryogenic memory, IEEE Trans. Appl. Supercond. **23**, 1701208 (2013).

[10] R. Caruso, D. Massarotti, V. V. Bolginov, A. Ben Hamida, L. N. Karelina, A. Miano, I. V. Vernik, F. Tafuri, V. V. Ryazanov, O. A. Mukhanov, and G. P. Pepe, RF assisted switching in magnetic Josephson junctions, J. Appl. Phys. **123**, 133901 (2018).

[11] R. Caruso, D. Massarotti, A. Miano, V. V. Bolginov, A. B. Hamida, L. N. Karelina, G. Campagnano, I. V. Vernik, F. Tafuri, V. V. Ryazanov, O. A. Mukhanov, and G. P. Pepe, Properties of ferromagnetic Josephson junctions for memory applications, IEEE Trans. Appl. Supercond. **28**, 1800606 (2018).

[12] B. Baek, W. H. Rippard, S. P. Benz, S. E. Russek, and P. D. Dresselhaus, Hybrid superconducting-magnetic memory device using competing order parameters, Nat. Commun. **5**, 3888 (2014).

[13] T. Golod, A. Iovan, and V. M. Krasnov, Single Abrikosov vortices as quantized information bits, Nat. Commun. **6**, 8628 (2015).

[14] I. M. Dayton, T. Sage, E. C. Gingrich, M. G. Loving, T. F. Ambrose, N. P. Siwak, S. Keebaugh, C. Kirby, D. L. Miller, A. Y. Herr, Q. P. Herr, and O. Naaman, Experimental demonstration of a Josephson magnetic memory cell with a programmable π-junction, IEEE Magn. Lett. **9**, 1 (2018).

[15] I. P. Nevirkovets and O. A. Mukhanov, Memory Cell for High-Density Arrays Based on a Multiterminal Superconducting-Ferromagnetic Device, Phys. Rev. Applied **10**, 034013 (2018).

[16] B. M. Niedzielski, T. J. Bertus, J. A. Glick, R. Loloee, W. P. Pratt, and N. O. Birge, Spin-valve Josephson junctions for cryogenic memory, Phys. Rev. B **97**, 024517 (2018).

[17] A. E. Madden, J. C. Willard, R. Loloee, and N. O. Birge, Phase controllable Josephson junctions for cryogenic memory, Supercond. Sci. Technol. **32**, 015001 (2019).

[18] N. Satchell, P. M. Shepley, M. Algarni, M. Vaughan, E. Darwin, M. Ali, M. C. Rosamond, L. Chen, E. H. Linfield, B. J. Hickey, and G. Burnell, Spin-valve Josephson junctions with perpendicular magnetic anisotropy for cryogenic memory, Appl. Phys. Lett. **116**, 022601 (2020).

[19] W. M. Martinez, W. P. Pratt, and N. O. Birge, Amplitude Control of the Spin-Triplet Supercurrent in $S/F/S$ Josephson Junctions, Phys. Rev. Lett. **116**, 077001 (2016).

[20] J. A. Glick, V. Aguilar, A. B. Gougam, B. M. Niedzielski, E. C. Gingrich, R. Loloee, W. P. Pratt, and N. O. Birge, Phase control in a spin-triplet squid, Sci. Adv. **4**, eaat9457 (2018).

[21] R. de Andrés Prada, T. Golod, O. M. Kapran, E. A. Borodianskyi, C. Bernhard, and V. M. Krasnov, Memory-functionality superconductor/ferromagnet/superconductor junctions based on the high-T_c cuprate superconductors $YBa_2Cu_3O_{7-x}$ and the colossal magnetoresistive manganite ferromagnets $La_{2/3}X_{1/3}MnO_{3+\delta}$ (X = Ca, Sr), Phys. Rev. B **99**, 214510 (2019).

[22] M. Weigand, B. Van Waeyenberge, A. Vansteenkiste, M. Curcic, V. Sackmann, H. Stoll, T. Tyliszczak, K. Kaznatcheev, D. Bertwistle, G. Woltersdorf, C. H. Back, and G. Schütz, Vortex Core Switching by Coherent Excitation with Single In-Plane Magnetic Field Pulses, Phys. Rev. Lett. **102**, 077201 (2009).

[23] V. Uhlíř, M. Urbánek, L. Hladík, J. Spousta, M. Y. Im, P. Fischer, N. Eibagi, J. J. Kan, E. E. Fullerton, and T. Šikola, Dynamic switching of the spin circulation in tapered magnetic nanodisks, Nat. Nanotechnol. **8**, 341 (2013).

[24] M. Kammerer, M. Weigand, M. Curcic, M. Noske, M. Sproll, A. Vansteenkiste, B. Van Waeyenberge, H. Stoll, G. Woltersdorf, C. H. Back, and G. Schuetz, Magnetic vortex core reversal by excitation of spin waves, Nat. Commun. **2**, 279 (2011).

[25] J. Linder and J. W. A. Robinson, Superconducting spintronics, Nat. Phys. **11**, 307 (2015).

[26] M. Eschrig and T. Löfwander, Triplet supercurrents in clean and disordered half-metallic ferromagnets, Nat. Phys. **4**, 138 (2008).

[27] G. Yang, C. Ciccarelli, and J. W. A. Robinson, Boosting spintronics with superconductivity, APL Mater. **9**, 050703 (2021).

[28] K. Lahabi, M. Amundsen, J. A. Ouassou, E. Beukers, M. Pleijster, J. Linder, P. Alkemade, and J. Aarts, Controlling supercurrents and their spatial distribution in ferromagnets, Nat. Commun. **8**, 2056 (2017).

[29] R. Fermin, D. van Dinter, M. Hubert, B. Woltjes, M. Silaev, J. Aarts, and K. Lahabi, Superconducting triplet rim currents in a spin-textured ferromagnetic disk, Nano Lett. **22**, 2209 (2022).

[30] See Supplemental Material at http://link.aps.org/supplemental/10.1103/PhysRevResearch.4.033136 for complementary data sets and a detailed description of our numerical approach for quantifying local stray fields.

[31] Samples with higher I_c values do show a Fraunhofer interference pattern, indicating a uniform distribution of I_c throughout the weak link.

[32] A. Singh, C. Jansen, K. Lahabi, and J. Aarts, High-Quality CrO_2 Nanowires for Dissipation-Less Spintronics, Phys. Rev. X **6**, 041012 (2016).

[33] R. S. Keizer, S. T. B. Goennenwein, T. M. Klapwijk, G. Miao, G. Xiao, and A. Gupta, A spin triplet supercurrent through the half-metallic ferromagnet CrO_2, Nature (London) **439**, 825 (2006).

[34] M. S. Anwar, F. Czeschka, M. Hesselberth, M. Porcu, and J. Aarts, Long-range supercurrents through half-metallic ferromagnetic CrO_2, Phys. Rev. B **82**, 100501(R) (2010).

[35] The length of the trench in the disk-shaped devices is typically between 1 and 1.6 μm, whereas the trench length of the ellipse devices presented here is less than 600 nm.

[36] X. Song, J.-P. Chen, Z.-P. Hou, M.-H. Qin, X.-S. Gao, and J.-M. Liu, Strain-mediated voltage-controlled magnetic double-vortex states in elliptical nanostructures, J. Magn. Magn. Mater. **547**, 168729 (2022).

[37] A. Vansteenkiste, J. Leliaert, M. Dvornik, M. Helsen, F. Garcia-Sanchez, and B. Van Waeyenberge, The design and verification of MuMax3, AIP Adv. **4**, 107133 (2014).